Comparisons of electron fluxes measured in the crustal fields at Mars by the MGS magnetometer/electron reflectometer instrument with a B field−dependent transport code

Michael W. Liemohn,[1] David L. Mitchell,[2] Andrew F. Nagy,[1] Jane L. Fox,[3] Tamara W. Reimer,[4] and Yingjuan Ma[1]

[1] We compare Mars Global Surveyor (MGS) magnetometer/electron reflectometer data with results from a B field−dependent kinetic transport code for "superthermal" electrons. The photoelectrons created on crustal field loops, when they are on the dayside, allow for the exploration of the magnetic topology and the upper atmospheric density structure. A case study of a typical orbit of the MGS satellite through the strong crustal field region in the southern hemisphere of Mars is examined. The results indicate that the low solar wind dynamic pressure during the selected orbit allowed for the expansion of the crustal field line to relatively high altitudes. Another feature of the photoelectrons in the crustal field region is that the distribution at high energies ($E > 100$ eV) is far more isotropic than what is expected from collisional scattering processes alone. Several candidate processes are discussed that might be preferentially scattering high-energy electrons. A final conclusion is that a two-stream model is inadequate for effectively examining photoelectron pitch angle distributions at Mars in the presence of the crustal fields. *INDEX TERMS:* 5435 Planetology: Solid Surface Planets: Ionospheres (2459); 5443 Planetology: Solid Surface Planets: Magnetospheres (2756); 2459 Ionosphere: Planetary ionospheres (5435, 5729, 6026, 6027, 6028); 2756 Magnetospheric Physics: Planetary magnetospheres (5443, 5737, 6030); *KEYWORDS:* photoelectrons, plasma transport, Mars, magnetic fields

1. Introduction

[2] The definitive observation of crustal magnetic fields on Mars [*Acuña et al.*, 1998] by the Magnetometer/Electron Reflectometer (MAG/ER) instrument [*Acuña et al.*, 1992] carried by the Mars Global Surveyor (MGS) has significantly changed our understanding of the plasma environment around this planet. Quantification of the crustal fields has shown that Mars actually has an unexpectedly complex interaction with the solar wind [e.g., *Acuña et al.*, 1999; *Connerney et al.*, 1999; *Purucker et al.*, 2000; *Ness et al.*, 2000; *Crider et al.*, 2000; *Ma et al.*, 2002]. Crustal fields are not a unique feature of a dynamoless planetary body, with similar observations at the Moon [*Lin et al.*, 1998], including the formation of "minimagnetospheres." However, the surface fields at Mars are "∼1000 times as strong," [*Lin et al.*, 1998, p. 1480], and the large field strength, combined with weaker solar wind parameters and the presence of a planetary atmosphere, makes the Mars minimagnetosphere a noticeable barrier for the solar wind over certain regions of the planet.

[3] Alternating polarity magnetic sources have been identified in the southern hemisphere [see *Connerney et al.*, 1999, Figure 3], with fields that can extend up over 1000 km above the planet. The crustal fields are strongest (up to 220 nT at the ∼400 km mapping phase altitude) over some of the oldest parts of the southern hemisphere [*Connerney et al.*, 2001]. *Ness et al.* [2000] cross correlated the crustal field observations with previous Mars plasma measurements, finding great consistency between the data sets and confirming that these fields are responsible for many of the unusual features of Mars' ionosphere. Phobos 2 data have also been reanalyzed in light of the MGS field measurements, finding anomalous plasma signatures that are probably the result of crustal fields [*Szego*, 2000].

[4] Important discoveries about the electrons near Mars have come from the MGS mission. For instance, the observation of ionospheric-type electron spectra above the ionopause allowed *Crider et al.* [2000] to study the

[1]Space Physics Research Laboratory, University of Michigan, Ann Arbor, Michigan, USA.
[2]Space Sciences Laboratory, University of California, Berkeley, California, USA.
[3]Department of Physics, Wright State University, Dayton, Ohio, USA.
[4]Physics Department, Harvey Mudd College, Claremont, California, USA.

effects of impact ionization of the neutral exosphere on the mantle region. Mass loading of the shocked solar wind increases the effectiveness of the magnetic pileup barrier [*Crider et al.*, 2002]. The MGS ER instrument has a large energy range, which allows a number of new observations to be carried out (e.g., Auger electrons [*Mitchell et al.*, 2000a]). Photoionization by X rays produces Auger electrons, and they are primarily formed in the ionosphere, making them a good delineator of spatial boundaries. Using this electron feature and other indicators in the MAG/ER data, *Mitchell et al.* [2000b, 2001] showed that the crustal magnetic field regions of the Martian southern hemisphere cause significant variations in the ionopause altitude (as defined by the photoelectron boundary, the local height to which the photoelectron spectrum dominates the ER measurements). The photoelectron boundary variability is also directly influenced by the solar EUV flux, the solar wind pressure, and the interplanetary magnetic field orientation.

[5] The MGS ER data set is rich with electron distribution function features that are difficult to explain without the employment of a numerical model. Its energy range, from 10 eV to 20 keV, allows for good observation of ionospheric and solar wind electrons in the suB keV superthermal range. ER's pitch angle resolution is good enough to distinguish between flowing streams of electrons and those trapped in local magnetic bottles. Its dynamic range is sensitive enough to detect the various electron populations surrounding Mars. With the accompanying vector magnetic field information the MAG/ER data set is well suited for studying the behavior of electron fluxes in the complex magnetic field environment at Mars.

[6] The unique interaction of the solar wind with the Martian ionosphere requires a sophisticated theoretical description. The most common type of hot electron transport code used in space physics is the two-stream model [*Nagy and Banks*, 1970], which does not take into account variations in the magnetic field. Two-stream models have been used extensively to explain the electron environments of several planets [e.g., *Nagy and Banks*, 1970; *Chen et al.*, 1978; *Gan et al.*, 1990]. Other numerical approaches with comparable pitch angle resolution to the two-stream model have also been used to study Mars electrons [e.g., *Fox and Dalgarno*, 1979; *Rohrbaugh et al.*, 1979; *Link*, 1999; *Seth et al.*, 2002]. Multistream methods (those with more than two pitch angle bins) have also been used to describe planetary electron environments, including Mars [e.g., *Mantas and Hanson*, 1979], but again, the assumption of a uniform magnetic field strength raises concerns about appropriateness for the complex field structure around Mars. The Martian environment stretches the validity of these types of models because of the strongly varying magnetic fields. Proper numerical investigation requires a better model to appropriately describe the electron flux behavior.

[7] Such a model exists and has been applied to the interhemispheric transport of photoelectrons in the Earth's ionosphere and plasmasphere [*Khazanov and Liemohn*, 1995; *Liemohn et al.*, 1997a]. The study presented here gives the initial results of the model after adaptation for the Mars environment. It is applied to the analysis of velocity space distributions in the strong crustal field region in the southern hemisphere of Mars, especially for investigating the observed pitch angle anisotropies.

2. MGS MAG/ER Data of the Crustal Field Structures on the Dayside

[8] MGS has been held to a 0200–1400 LT Sun-synchronous orbit that is nearly circular (370–430 km altitude range) since the beginning of the mapping phase of the mission in March 1999. The strong crustal field region in the southern hemisphere is seen by MGS on both the dayside and the nightside on each Martian day. The MAG/ER data routinely indicate the presence of crustal fields and the extension of the ionosphere up to the satellite altitude. Therefore there is a vast collection of crustal field and high-altitude ionospheric data from MGS.

[9] A typical dayside pass over a strong crustal field region was made on the ninth orbit of 12 May 1999. This orbit is chosen for examination for several reasons: (1) It is near the beginning of the mapping phase, and thus the instrument has not undergone any significant sensitivity degradation; (2) its orbit track is perpendicular to several of the magnetic arcade structures, thus increasing the chance of observing magnetically conjugate points along the field lines; and (3) the solar wind dynamic pressure (as extracted from the morphology of the magnetic pileup region, seen in the pass over the northern hemisphere) is low, making this orbit a good choice for quantifying the nominal magnetic field configuration. Figure 1 is a summary plot of this orbit, showing several ephemeris values (altitude, latitude, longitude, and solar zenith angle) as well as several measurements from the MAG/ER (magnetic field strength and dip angle and the pitch angle-averaged electron fluxes for a few energy channels). The strong crustal field regions are clearly identifiable. In general, the spikes in the field strength are coincident with nearly vertical magnetic field lines, indicating that MGS is flying directly above one of the magnetized regions. During the crustal field overflight interval the electron fluxes are distinctly different from the rest of the orbit. The values are nearly constant (at least on the chosen scale), a feature that is unique to the crustal field region. Such constancy is a typical signature of the ionospheric photoelectrons, including the Auger electrons in the hundreds of eV range [e.g., *Mitchell et al.*, 2000a]. Figure 1h shows the satellite position as a function of latitude and longitude, with a dotted-line box indicating the general region of Mars where the crustal fields are strongest [e.g., *Acuña et al.*, 2001, Plate 2].

[10] An interesting feature seen in Figure 1a is a brief enhancement of the electron fluxes during the crustal field interval (near 1610 UT). It is seen that the flux levels are consistent with the sheath distribution, measured before 1600 UT and after 1630 UT. This measurement of magnetosheath electrons is an example of a cusp feature. The magnetic field is nearly vertical during the magnetosheath electron observations, giving the solar wind direct entry into the ionosphere. The interval is short-lived: <15 s, indicating a width of <50 km at 380 km altitude. The peak of the flux spike is even narrower. While a detailed discussion of electron population intermixing will not be given here, its existence illustrates complicated interactions of the solar wind with the crustal fields at Mars.
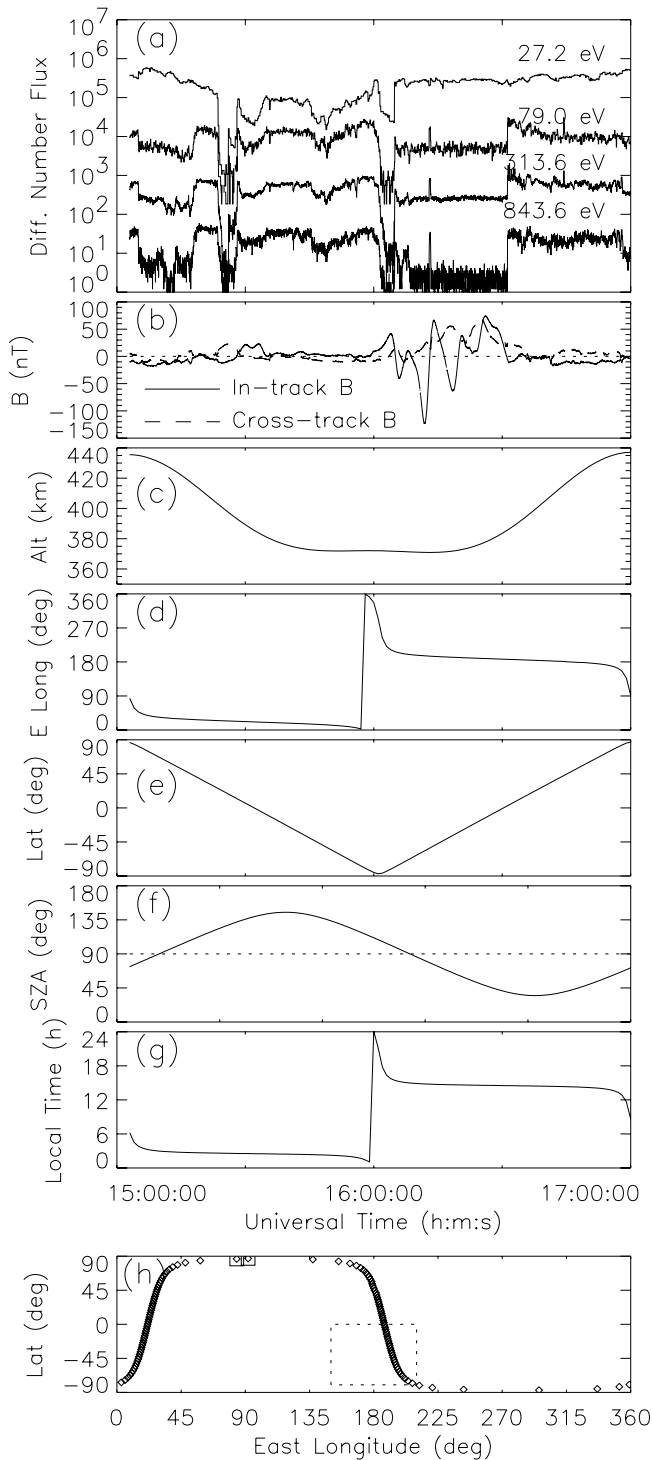
Figure 1. MGS data for orbit 9 on 12 May 1999. Shown are (a) pitch angle-averaged differential number flux for four energy channels; (b) two components of the magnetic field vector (in track means along the MGS velocity vector, and cross track means the horizontal field that is perpendicular to the MGS velocity); (c) MGS altitude; (d) MGS location over Mars in east longitude; (e) MGS location of Mars in latitude; (f) MGS solar zenith angle (the 90° value is highlighted with a dotted line); (g) MGS local time at Mars; and (h) the position of MGS over Mars in both latitude and longitude (the two square symbols mark the start and end apoapsis positions).

[11] Figure 2 presents a close-up view of the flight over the strong crustal field region during the dayside portion of the orbit (tick marks are now 10 min apart instead of 30 min as in Figure 1). The magnetic field data are presented two ways. Figures 2a–2c show it in spherical coordinates, with elevation angle being the up-down direction of the field (positive when the field is directed away from the planet) and azimuthal angle being the horizontal direction of the field (positive is to the left of the spacecraft, here westward because MGS is flying northward). Figures 2d and 2e show the field as two sets of normalized vectors (arbitrarily chosen scale but the same for both plots). Figure 2d shows the component in the plane of the orbit track (upward fields are positive, and northward fields are tilted toward the right), and Figure 2e shows the component perpendicular to the orbit track (westward fields are positive). The absolute magnitudes of these two unit vector components are shown in Figure 1b (in track and cross track for Figures 2d and 2e, respectively). Figure 2d clearly demonstrates the looping structuring of the magnetic field. The in-track component systematically gyrates as the satellite cuts through the magnetic arcades. Two of the crustal field arcade crossings are marked with three dots each: one on their southern legs, one near the center where the field is horizontal, and one on their northern legs. The electron data at these six points will be shown below. It is seen that the elevation angle performs a smooth rotation through each arcade (each set of three points) and the azimuthal angle is relatively constant through each set as well.

[12] Figure 3 shows the pitch angle-averaged differential number fluxes of the observed electrons at the six points highlighted in Figure 2. It is seen that the spectra are quite similar, regardless of latitude or relative location along the crustal field line. Typical photoelectron features are seen in the spectra. The slight bump in the 20–30 eV range is from electrons generated by the very intense He II 30.4 nm solar line (~40 eV). The knee in the distribution from 50 to 70 eV is from the sharp drop in solar photons below 15 nm. The slight bumps in the distribution near 150 eV and 500 eV are from Auger (inner shell) electron production by soft X rays. The abrupt cutoff of the spectrum around 500 eV is also a characteristic feature of the atmospheric photoelectron spectrum for the terrestrial planets, as the source term is extremely small for energies beyond the last Auger peak. It is clear from Figure 3 that all six points are below the photoelectron boundary and the spectra are essentially free of solar wind electron contamination.

[13] Figure 3 taken by itself implies that the photoelectrons on the crustal field lines are rather uninformative about the magnetic topology around Mars. MGS, however, provides another dimension (literally) to the electron distribution function: pitch angle. Figure 4 shows the two-dimensional velocity space distributions (energy versus pitch angle) of differential number flux for the six locations marked in Figure 2. Figures 4a and 4e show the pitch angle-averaged fluxes again for reference (in histogram mode). The two dashed lines on Figures 4b–4d and 4f–4h denote the pitch angle extent that MAG/ER was able to measure at each time.

[14] Let us briefly explain the pitch angle extents shown in Figure 4. The ER instrument is body mounted on the "side" of MGS so that the hemispheric cap of ER is pointed
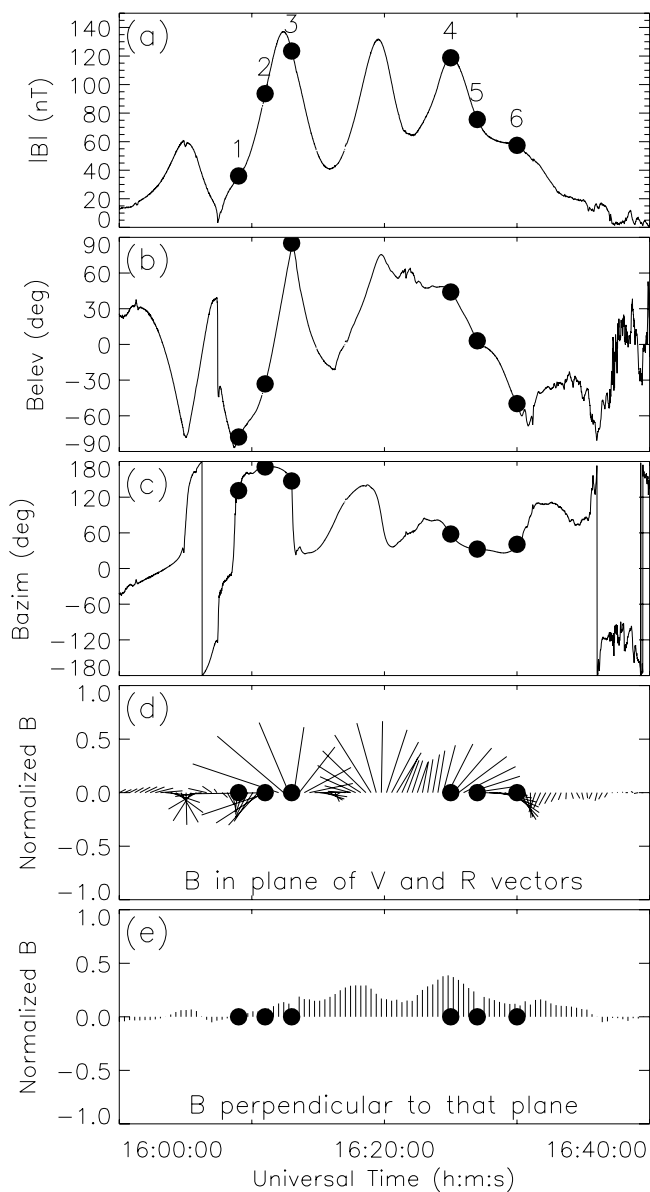
Figure 2. MGS data during the overpass of the crustal field region of orbit 9 on 12 May 1999. Shown are (a) magnetic field magnitude; (b) magnetic field elevation angle (0° is horizontal, −90° is down, and +90° is up); (c) magnetic field azimuthal angle (0° is in the direction of MGS motion, 90° is to the left, 180° is opposite of MGS motion, and 270° is to the right); (d) normalized magnetic field component in the plane made by the MGS velocity vector and local vertical; and (e) normalized magnetic field component in the direction to the right or left of MGS (relative to the MGS velocity vector). The six dots in each panel are at the six locations highlighted in Figures 3–5.

80° to the left of the mapping phase velocity vector (on the west side of MGS during the northward flying dayside portion of the orbit). Therefore the viewable portion of the pitch angle range changes as the magnetic field changes elevation and azimuthal angle. Locally mirroring particles are always seen, while perfectly field-aligned particles are only seen when the field line vector is parallel to the

plane of the anode ring. Thus a vertical or north-south directed field line allows MGS to sample nearly all pitch angles, while an east-west directed field line shrinks the observed pitch angle range to a small interval around 90°. The relationship between observed pitch angle extent and the magnetic field direction is demonstrated by comparing the field elevation and azimuthal angles shown in Figures 2b and 2c with the pitch angle extents shown in Figures 4b–4d and 4f–4h.

[15] A feature that is seen in Figures 4b–4d and 4f–4h is that the pitch angle distributions at low energies ($E < 70$ eV) are anisotropic. The fluxes along the magnetic field line (near 0° and 180°) are higher than the locally mirroring fluxes (near 90°). The difference can be as large as a factor of 4. A minimum at 90° is the expected anisotropy for particles with a "source cone" distribution. That is, the source of photoelectrons is primarily below 200 km altitude, but the satellite is orbiting at ∼400 km altitude. Because the photoelectrons are relatively fast, some can escape upward from the source region at one end of the field line and travel to the other (conjugate) ionospheric foot point of the field line. If there were no collisions above 200 km, then the electrons would simply spiral along the field line and be deposited in the conjugate ionosphere. The magnetic field strength along the field line is not constant, however, so the electrons focus in pitch angle as the magnetic field strength weakens on the upward leg of the journey along the field line, and then the electrons broaden again as the field strengthens on the downward leg. The pitch angle focusing in weak field regions makes the distribution appear as a cone when examined in parallel-perpendicular velocity space, hence the name source cone. Adiabatic pitch angle focusing and broadening is not the only process acting on the electrons, however. Between the two source regions the electrons undergo collisions with whatever background neutral or plasma particle populations exist at the high altitudes. Some of the electrons therefore are scattered out of the "fly-through zone" (the source cone region of pitch angle space near 0° and 180°) and into the "trapped zone" (the region of pitch angle space that mirrors above 200 km). Because electrons in the trapped zone will mirror before reaching the collision-dominated low-altitude portion of the field line, they could survive a long time in the magnetic bottle along the field line. However, the trapped zone flux is invariably lower than the source cone flux supplying it, and therefore an anisotropic distribution arises.

[16] Note that the anisotropies shown in Figure 4 are thought to be real, physical anisotropies and not an artifact of spacecraft or instrumental influences. The ubiquity of source cone distributions over the crustal fields and their absence at other times of the orbit indicate that the observed source cone distributions are real physical features. That said, the low-energy range of the MAG/ER electron data can be affected by localized electric potentials from differential charging around the spacecraft chassis, so the anisotropies could be biasing artifacts. Spacecraft charging is well understood, however, and it is known which sectors of the pitch angle map are most influenced by the spurious electric fields. To avoid the possibility of contamination, the lower of the two flux values for each pitch angle bin is used in the data analysis (because of the geometry of the instrument, each pitch angle is sampled twice; please see
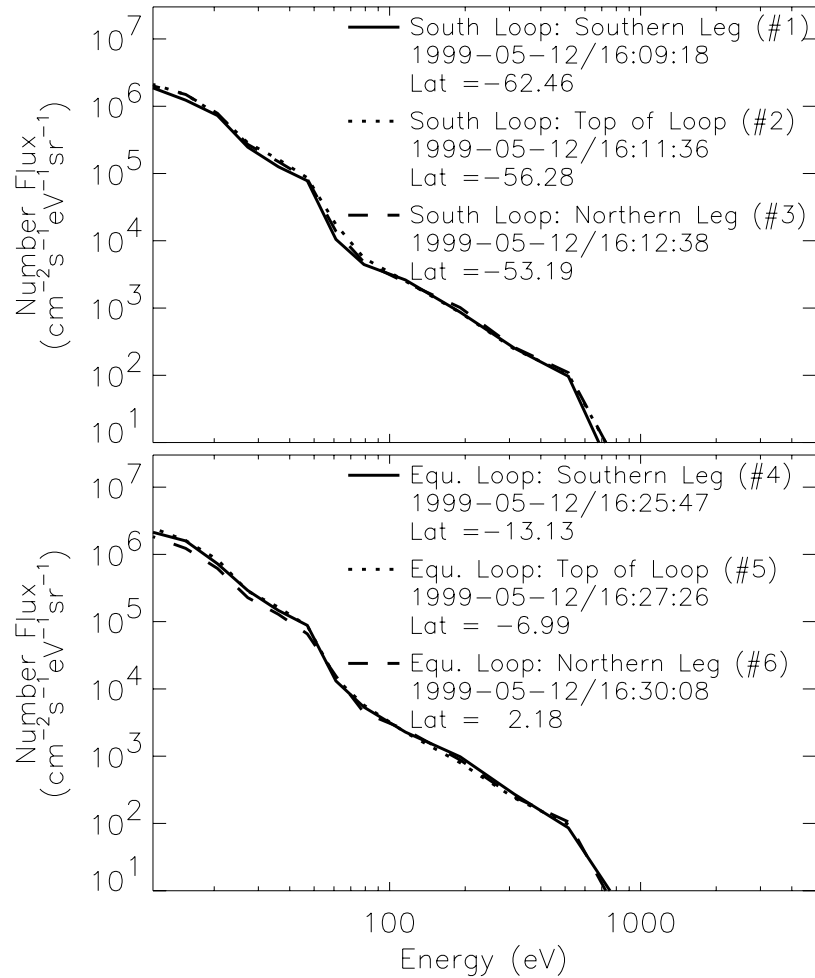
Figure 3. Pitch angle-averaged energy spectra of differential number fluxes at the three points in the (top) southern and (bottom) equatorial loops.

Acuña et al. [1992] and *Mitchell et al.* [2001] for more details about spacecraft charging effects on ER). That is, any deviations from gyrotropy (differences between the two flux values for the same pitch angle) are assumed to be from enhancements caused by the localized electric potentials. Therefore all of the fluxes at low energies are actually a lower limit to the real flux of photoelectrons in the Mars ionosphere.

[17] Figure 5 shows pitch angle distributions of the observed differential electron flux at the six selected locations for the energy bin centered at 15 eV. The bold lines are the measured fluxes, while the two thin lines on either side of each bold line are the 1-sigma uncertainty estimates of the observed values. As in Figure 4, the plotted fluxes are the lower of the two flux values for each pitch angle, as discussed in the previous paragraph. The source cone distribution is evident, especially in Figures 5a, 5c, and 5f where the magnetic field is nearly vertical and the error bars indicate that the anisotropies are statistically significant. When the magnetic field is horizontal (Figures 5b and 5e), the pitch angle distribution is more isotropic. The high-energy distributions (not shown) are quite flat and usually have larger error bars owing to the lower count rates.

[18] The systematic decrease in the trapped zone flux relative to the source cone flux can be used to explain some observed features in the pitch angle-averaged flux spectra. For instance, the MGS MAG/ER data occasionally show a slight decrease in the pitch angle-averaged photo-electron flux level (a "dropout") when flying over the crustal field regions. Figure 6 presents an example of one such observation. The averaged spectra before and after the dropout are nearly identical, but the averaged spectrum during the dropout is noticeably lower for $E < 70$ eV. The ratio of the flux before the dropout to the flux during the dropout is 0.711 over the range from 10 to 50 eV. Figures 6b–6d offer some explanation of the decrease. Figure 6c shows that during the dropout, MAG/ER was only sampling a small portion of the pitch angle distribution, namely, the center of the trapped zone. Before and after the dropout the field line vector was oriented such that MAG/ER observed a larger part of the pitch angle spectrum. Therefore it can be concluded that the anisotropy of the source cone distribution created the brief decrease in the pitch angle-averaged fluxes.

[19] The example in Figure 6 shows that the pitch angle-averaged fluxes from MGS are only averages over the observed section of the pitch angle range. The observed
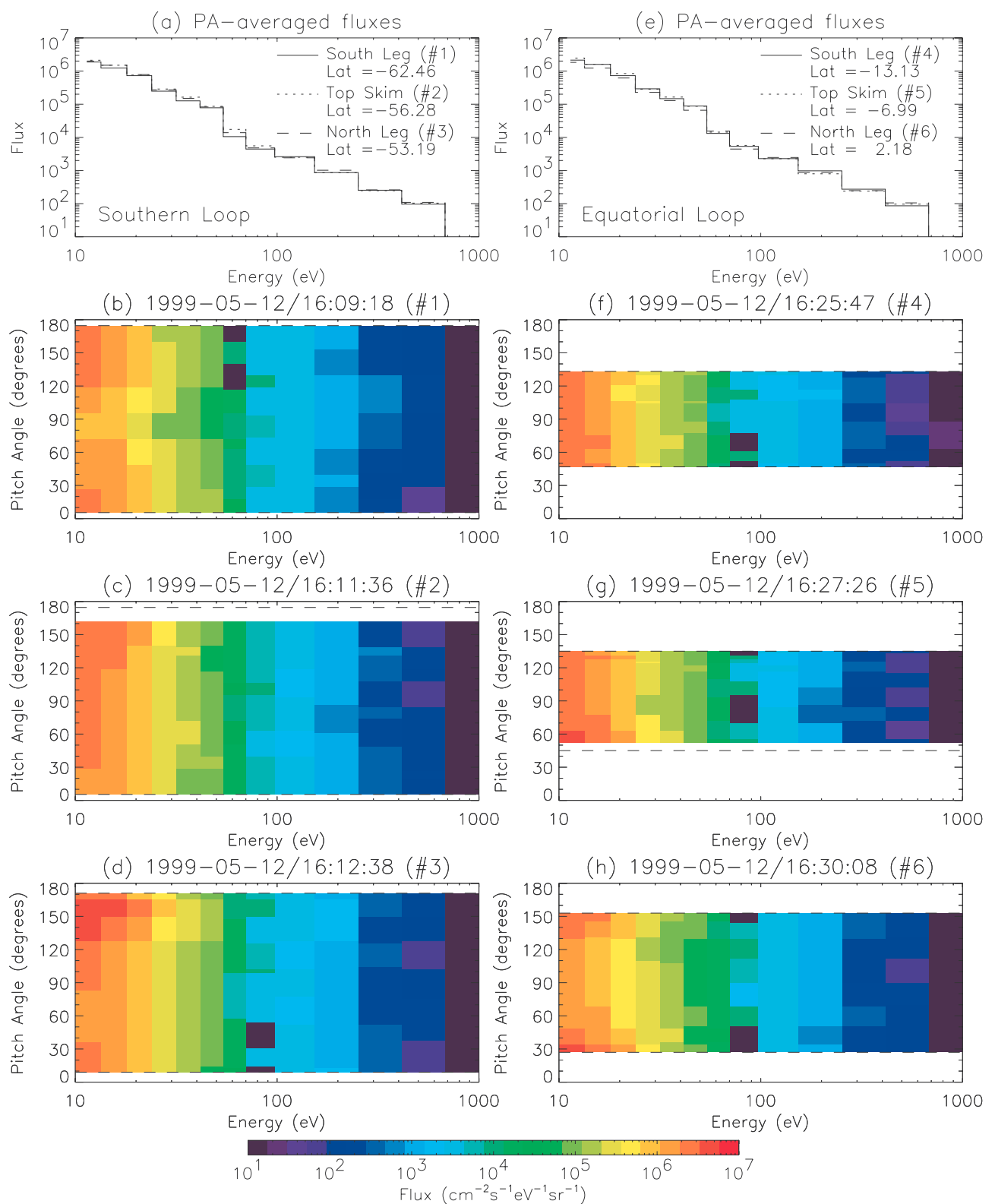
Figure 4. Energy-pitch angle (PA) spectrograms at three points in the (left) southern and (right) equatorial loops. Pitch angle-averaged spectra are shown in top graphs.
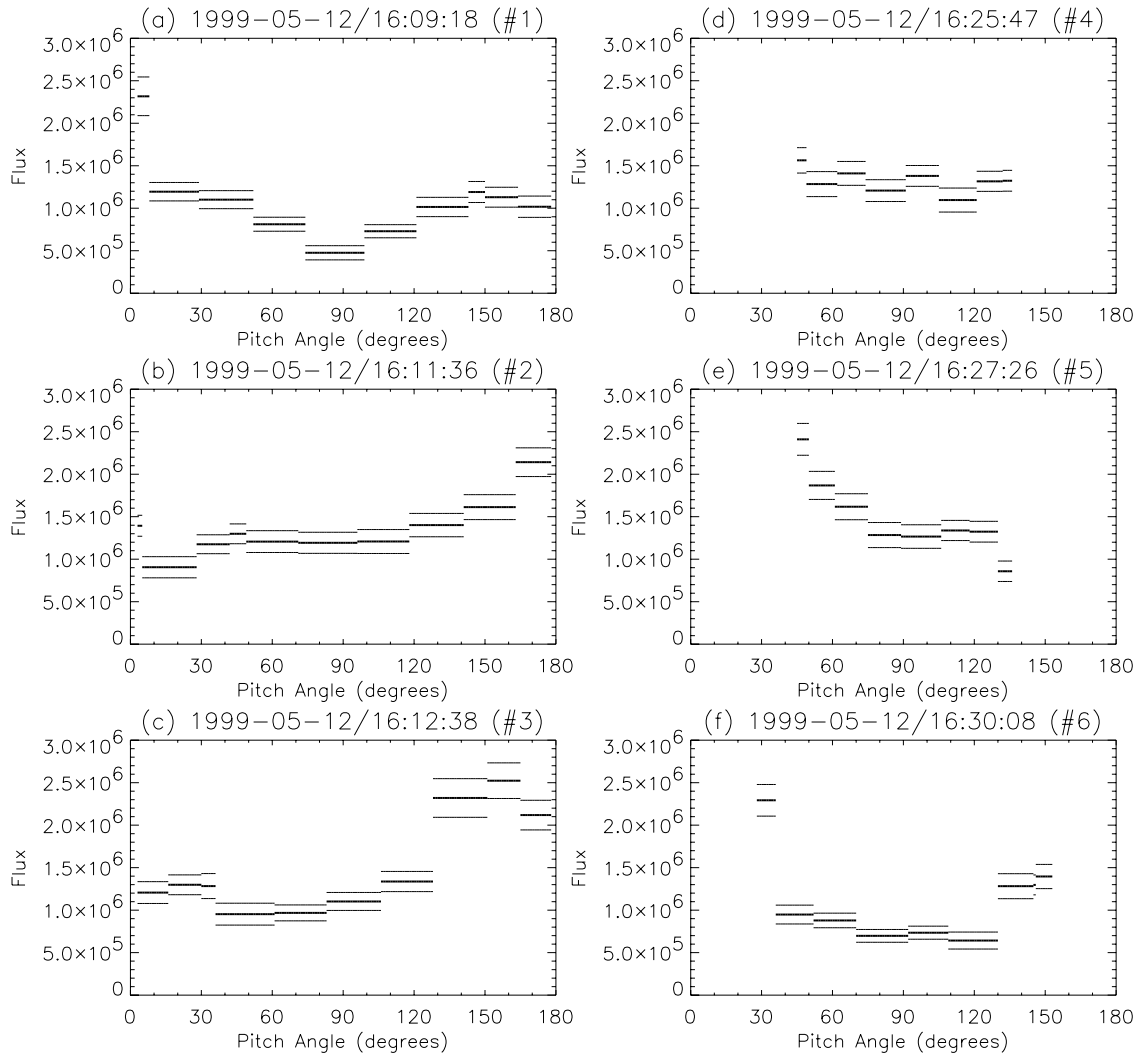
Figure 5. Pitch angle distributions at the three points in the (left) southern and (right) equatorial loops for the energy bin centered at 15 eV. The bold lines are the data, and the two thin lines above and below each bold line are the 1-sigma uncertainty estimates.

range varies as the magnetic field vector rotates relative to the ER detector plane. Over the crustal field regions, where source cone anisotropies are the norm, the observationally determined pitch angle-averaged fluxes should be considered lower limits of the true pitch angle-averaged fluxes ("true" being the average flux in the limit that all 180° are known).

[20] The point of showing all of these data is to demonstrate that the photoelectron distributions over the crustal field regions at Mars contain pitch angle anisotropies. Moreover, quantitative information about the magnetic topology and the upper atmospheric densities can be extracted from numerous quantities in the velocity space distribution, most notably from the following parameters: width of the trapped zone, extent of the trapping (flux ratios), angle of the sharp drop in flux with energy (for collisional processes, lower energy electrons are scattered more readily than higher-energy electrons), and amount of electrons traversing the magnetosphere into the conjugate ionosphere (assuming both endpoints of a field line are observed).

[21] As discussed in section 1, the common modeling approach of using a two-stream electron transport code is insufficient for numerical examination of pitch angle anisotropies. By definition, a two-stream calculation only produces hemispherically averaged (upward and downward) energy spectra. Therefore a multistream transport model is more appropriate for the task. The model, however, must include the effects of magnetic strength variations along the field line to be useful in quantitatively examining the measured electron fluxes shown above. Such a model exists for Earth, and the objective of the present study is to show the initial analysis of the electron velocity space distribution at Mars using this electron transport code.

3. Numerical Model

[22] A model has been developed that calculates the superthermal electron distribution function in the Earth's ionosphere-magnetosphere system [*Khazanov et al.*, 1993; *Khazanov and Liemohn*, 1995; *Liemohn et al.*, 1997a]. It simulates hot electron transport along a magnetic field line
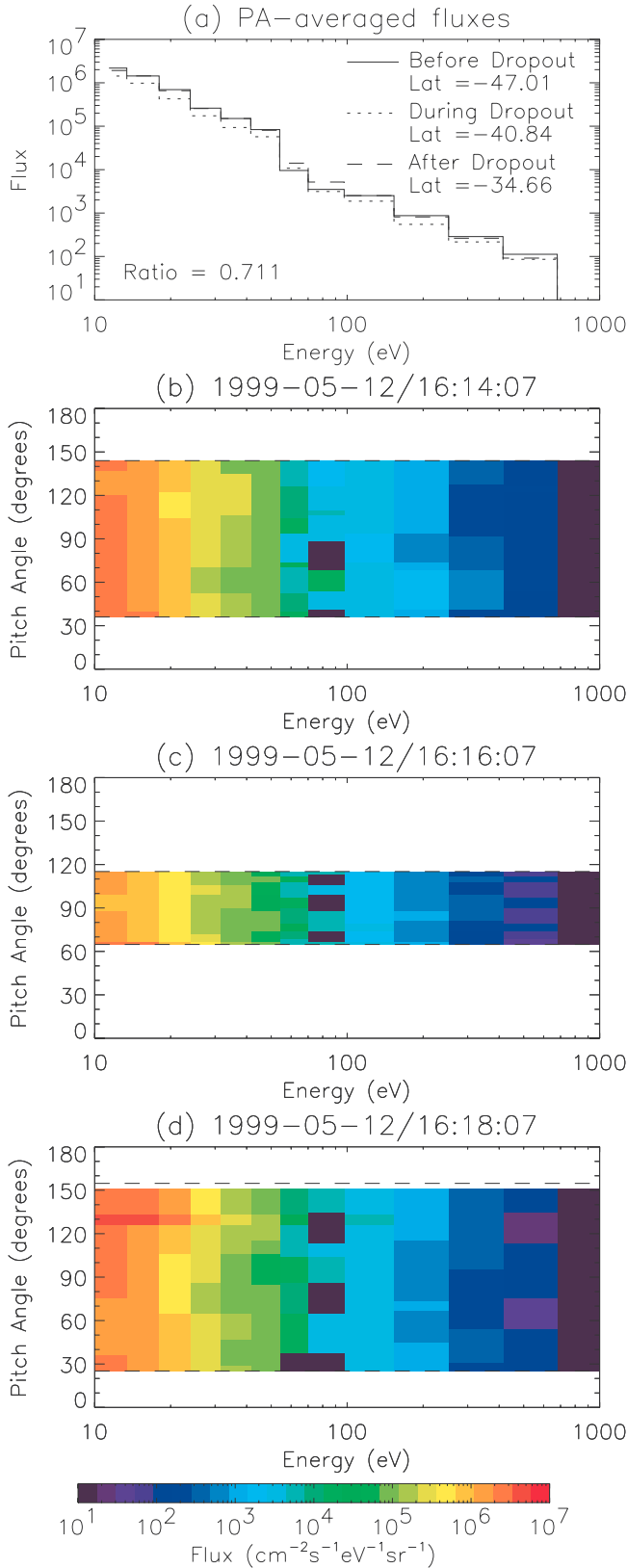
Figure 6. Pitch angle-averaged spectra and the energy pitch angle spectrograms for three times around a "flux dropout" event (before, during, and after) during the crustal field overflight on this orbit.

by calculating the time-dependent superthermal electron distribution function, f, from the gyration-averaged kinetic equation [e.g., *Liemohn et al.*, 1997a]:

$$\sqrt{\frac{m}{2E}}\frac{\partial \phi}{\partial t} + \mu\frac{\partial \phi}{\partial s} - \frac{1-\mu^2}{2}\left(\frac{1}{B}\frac{\partial B}{\partial s} - \frac{F}{E}\right)\frac{\partial \phi}{\partial \mu} + EF\mu\frac{\partial \phi}{\partial E} = Q + S,$$

$$(1)$$

where $\phi = 2Ef/m^2$ is the superthermal electron flux; m is the electron mass; t is the time; s is the distance along the field line; E is the particle energy; and μ is the cosine of the local pitch angle α. The inhomogeneity of the geomagnetic field, B, is included, as well as other forces such as electric fields, in F (for the present study, F is assumed to be zero). Q is the superthermal electron source term (primary and secondary electron sources), and S includes the collision integrals, representing interactions with thermal electrons and ions, elastic scattering with neutral particles, inelastic excitation and ionization scattering with neutral particles, and wave-particle interactions. The model can be used with any neutral atmosphere, thermal plasma, and magnetic field model to calculate the electron flux. It uses the numerical technique of *Khazanov et al.* [1984], which replaces the derivatives with second-order accurate advection and diffusion schemes. The generality of the background magnetic field allows for the calculation of open field line transport as well as closed field line plasma motion. From the resulting distribution functions the energy deposition to the thermal plasma and neutral atmosphere can be easily calculated, as well as the stability of the superthermal electron distribution.

[23] As discussed in section 2, electrons change their local pitch angle as they move through a magnetic field strength gradient (third term in equation (1)). If the kinetic equation is written in terms of the local pitch angle, then a non-Cartesian grid must be used in s-μ space to avoid the accumulation of numerical errors. It is therefore convenient to rewrite the kinetic equation in terms of μ_0, the pitch angle at the location of minimum B. The minimum B location is the place of maximum "focusing" of the pitch angle distribution; thus all pitch angles everywhere else along the field line can be mapped to some μ_0 value using the first adiabatic invariant,

$$\frac{1-\mu^2}{B} = \frac{1-\mu_0^2}{B_0},$$

$$(2)$$

where B_0 is the minimum magnetic field strength along the field line. Figure 7 shows schematics of the s-μ plane and s-μ_0 plane, indicating the fly-through regions and trapped zone regions for each variable set. After the transformation the $\partial B/\partial s$ term in equation (1) cancels, and a major source of numerical error is removed. Now a Cartesian grid can be used in s-μ_0 space, and the relatively slow collisional processes are the only things redistributing the electrons in μ_0.

[24] The code was designed to highlight the formation of the pitch angle distribution away from the source region of the particles. That is, the "slow" process of pitch angle scattering, included in the S term in equation (1), is the main physical process of interest that should be resolved. Note that the B field inhomogeneity is taken into account through
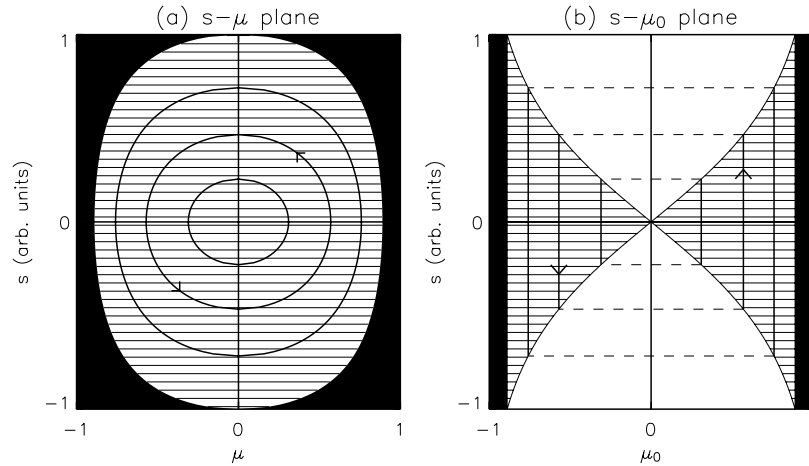
Figure 7. Schematics of superthermal electron trajectories as a function of spatial distance along the field line and pitch angle from the left-hand side of equation (1), showing (a) the trajectory dependence on local pitch angle (s-μ plane) and (b) the trajectory dependence on equatorial pitch angle (s-μ₀ plane). The solid region is the source/loss cone, in which particles reach the ionospheric foot points (s = ±1), the striped region is the trapped zone, in which particles mirror before the base of the field line, and the white regions (Figure 7b only) are forbidden areas outside of the region of existence, where no calculation is necessary. Several trapped zone trajectories are drawn for illustration.

a transformation back to local pitch angle. Equation (1) is therefore written as a diffusion equation,

$$\left(\sqrt{\frac{m}{2E}} \frac{\partial \phi}{\partial t} + \mu \frac{\partial \phi}{\partial s} + C_1 \frac{\partial \phi}{\partial E} \right) + C_2 \frac{\partial}{\partial \mu_0} \left(C_3 \frac{\partial \phi}{\partial \mu_0} \right) = Q. \quad (3)$$

In equation (3) the C_1, C_2, and C_3 coefficients include summations over species to account for the various neutral and plasma particles in the upper atmosphere of Mars. In equation (3) the spatial transport derivative and the energy degradation derivative assume a role analogous to the time derivative in a standard diffusion equation. Thus leaps to steady state are conducted by simply removing the time derivative term (that is, setting Δt equal to "infinity"), because the spatial and energy derivatives act like pseudotime derivatives in equation (3). The resulting scheme is not particularly well suited for resolving propagation fronts along the field line (dispersion will smear any initial sharpness), but it is very well suited for resolving the long-term development, evolution, and interplay between the source cones and the trapped zone. (See *Khazanov et al.* [1993] and *Khazanov and Liemohn* [1995] for additional information regarding the theoretical approach, the variable transformation, or the numerical technique used in the model.)

[25] Appropriate thermospheric and ionospheric parameters (e.g., densities) are needed for implementation of the transport code. The Mars thermospheric general circulation model (MTGCM) is used [*Bougher et al.*, 1988] for the neutral atmosphere. MTGCM continues to be updated with new information about the Martian upper atmosphere [e.g., *Bougher et al.*, 1994, 2001]. It provides altitude profiles of the major neutral species densities that are needed for both the photoelectron production calculation and the collisional interaction terms. The $F_{10.7}$ proxy value at Mars for the chosen day (12 May 1999) is relatively low; therefore a typical solar minimum atmospheric profile has been used, specifically the solar minimum Mars aphelion profiles from *Fox et al.* [1996]. Altitude profiles of the major ion species and the thermal electrons are also needed for the collisional terms and are taken from the same solar minimum case of *Fox et al.* [1996]. The solar photon flux used in the present study is that from the *Hinteregger et al.* [1981] model as scaled by $F_{10.7}$. The correction proposed by *Solomon et al.* [2001] is also applied, which quadruples the flux of photons for wavelengths below 20 nm.

[26] Another necessary input to the model is cross-section information. *Fox* [1991] compiled a comprehensive listing of the relevant photoionization and electron impact ionization and excitation cross sections for Mars and other planetary environments. The electron impact cross-section portion of the *Fox* [1991] review has recently been updated by *Sung and Fox* [2000]. These two surveys form the basis of the cross-section information used in the model.

[27] In order to proceed with the calculation a magnetic field model is needed. The approach chosen for the present study uses a series of magnetic strips of alternating polarity (upward and downward directed) on the planet surface. Using the magnetic field observations of *Acuña et al.* [1999] and *Connerney et al.* [1999, 2001] and the altitude-normalized map of the crustal fields by *Purucker et al.* [2000] and *Ness et al.* [2000], a reasonable representation of the crustal field line topology for the selected orbit on 12 May 1999 can be constructed. The implementation of the crustal field for a given arcade is therefore an east-west oriented quasi-two-dimensional dipole. Such a method is chosen rather than using one of the existing empirical descriptions of the field [*Purucker et al.*, 2000; *Arkani-Hamed*, 2001, 2002; *Cain et al.*, 2003], because the field configuration is taken to be a free parameter in the simulations. Several shapes and intensities of the field line are used to reach data-theory agreement in the electron velocity distributions.

[28] The phase-space distribution comparisons between the data and the model results are conducted as follows. The MGS ER instrument has an energy resolution of $\Delta E/E$ of 0.25 [*Acuña et al.*, 1992]. Model calculations can (and often need to) have much finer energy resolution. The pitch angle resolution can also be different; the measured pitch angle resolution of the ER instrument is up to 22.5° (depending on the magnetic field orientation), while the model resolution can go from 90° (two-stream approximation) to 1° (massively multistream). In the study presented here, the calculations were carried out with an energy resolution smaller than that of the data (varying from 1 to 10 eV, increasing with increasing energy). Pitch angle resolution in the model calculations varies from 2 up to 40 bins across the 180° range, depending on the local magnetic field strength relative to the minimum field strength along the field line. For the data-theory comparisons the model results are averaged into larger energy and pitch angle bins to match the resolution of the data. In this way, indistinct features in the data can be explained in terms of the fine-scale resolution of the more realistic electron distribution, as simulated by the model.

4. Data-Theory Comparison

[29] A complete and detailed comparison for all six points in Figures 2–5 discussed in section 2 is impractical and a bit redundant. Therefore only point 1, on the southern leg of the southern loop, will be examined here. However, it will be assumed that point 3 is the correct choice of the northern leg of the magnetic field loop, and therefore point 3 will also be used in defining the simulations.

4.1. Numerical Experiment Configurations

[30] In order to examine the crustal magnetic field topology and the upper atmospheric density profile at Mars the model was run with several different descriptions of these quantities to see which simulation result best matches the observations. Three different atmospheric density profile sets were employed. The first assumed solar minimum conditions when Mars is at aphelion, as was the case on 12 May 1999. The heliocentric distance of Mars for this day is 1.57 AU, near aphelion for the planet's orbit, and so the aphelion aspect of the selected atmospheric density choice is correct. The $F_{10.7}$ value for Mars was interpolated from the $F_{10.7}$ time series for Earth, taking into account the Earth-Sun-Mars angle. The $F_{10.7}$ value for 12 May 1999 was calculated to be 155.6, with an 81 day average value of 143.4. These two values are not particularly low, but they are closer to solar minimum than maximum. To test the solar cycle dependence, a second atmospheric density case was also used, assuming solar maximum conditions at Mars perihelion (also from the *Fox et al.* [1996] study). This second density profile choice puts an extreme upper bound on the upper atmospheric conditions. Note that the MTGCM does not extend up to the 400 km altitude of MGS, and so a scale height for each species is applied to extrapolate the model results beyond the MTGCM simulation domain. The difference in scale height between the solar minimum and solar maximum cases is a factor of roughly 1.6. As a third case a "below solar minimum"

atmosphere is also used, where the densities above the exobase (~200 km) are determined with a scale height that has been reduced by the same 1.6 factor as was found between the solar maximum and solar minimum cases. While such a profile is an unrealistically depleted upper atmosphere, it is a valuable exercise to illustrate the utility of the model and to place a lower bound on the data-theory comparisons.

[31] Several different choices of magnetic field topology were adopted for the calculations. The two chosen points (points 1 and 3 in Figures 2–5) for the times that MGS crossed the field line of interest are roughly 600 km apart. The magnetic field strengths 40 and 140 nT and elevation angles −73° and 60° at the southern and northern points, respectively, are known. Using these magnitude and angle values at 400 km, a magnetic field line with a given altitude dependence can be defined. The field strength from the northern source is given an altitude dependence of R^{-2} (two-dimensional dipole, resembling a horizontal bar magnetic configuration), while the exponent for the southern source is set to −3.9, −4.4, and −5.6 for three different field line profiles (compressed, nominal, and expanded, respectively). These exponent choices yield B field vectors that closely match the MGS magnetometer observations, with progressively higher field line apexes. The results of this exercise are shown in Figure 8. The solid line result is taken as the nominal field line description and is used with all three atmospheric density profiles. The dotted line and the dashed line results can be thought of as compressed and expanded field line descriptions, respectively. The three loop structures extend to 576 km (compressed), 752 km (nominal), and 870 km (expanded). A fourth B field strength definition, the horizontal dash-dotted line in Figure 8b, is used with the nominal loop configuration in Figure 8a. The level of the constant B field case is set to 90 nT, the average of the two observed B field values. Such a result will be analogous to using a two-stream code (to be precise, a multistream code with constant B).

[32] In order to estimate the compressional force on the field line from the solar wind a proxy for the solar wind dynamic pressure for any given orbit was created. In the northern hemisphere, where the crustal fields are quite weak, the photoelectron boundary is nearly always below the altitude of MGS. Therefore the satellite passes through part of the magnetic pileup region during the northbound (dayside) portion of the northern hemispheric traversal. The peak magnetic field strength measured in the magnetic pileup region is used to calculate a magnetic pressure, which is used as a proxy for the solar wind dynamic pressure. A cosine-squared term is applied to normalize the magnetic pressure [cf. *Vennerstrom et al.*, 2003] to a solar zenith angle of 30° (the minimum solar zenith angle observed by MGS in the mapping phase, owing to the 0200–1400 LT orbit). For the selected orbit the maximum normalized magnetic pressure was 0.066 nPa. Normalizing to 0° solar zenith angle yields 0.088 nPa. This value can be considered a lower limit for the solar wind dynamic pressure during the chosen orbit because other factors, such as atmospheric pressure, also contribute to the pressure balance relationship. *Vennerstrom et al.* [2003], however, concluded that the magnetic pileup region pro-
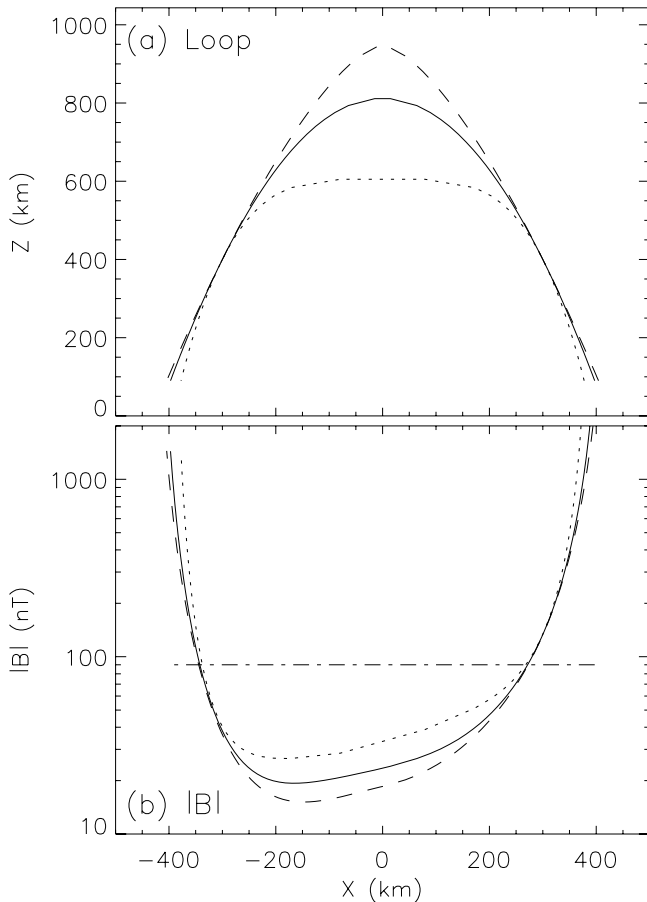
Figure 8. (a) Altitude (*z*) and latitude (*x*) dependence of the crustal magnetic field line specifications to be used in the simulations. (b) Magnetic field strength along the field line.

vides nearly all of the standoff pressure at Mars. However, it could also be that MGS did not pass through the absolute peak of the magnetic field in the pileup region. In addition, there are time-aliasing issues because of solar wind changes over the 2 hour MGS orbit period. Despite these caveats the calculated number is a rough approximation of the solar wind dynamic pressure and is sufficient for the present study.

[33] A solar wind dynamic pressure of 0.088 nPa is quite small, even for a heliocentric distance of 1.57 AU (the normal solar wind pressure here is roughly 1 nPa [*Luhmann and Brace*, 1991]). However, the calculated pressure is a lower limit because it only takes into account a single term (magnetic pressure). Therefore it is believed that the three field line topologies chosen for the simulations are reasonable end-member test cases. It is fair to assume, based solely on the $F_{10.7}$ and pressure proxies, that the nominal field line with a solar minimum atmosphere should yield the best match to the data. This field line has a high apex well above the satellite altitude and represents a slightly expanded field line. However, because the lower limit pressure proxy is more than a factor of 10 below normal, one could argue for the expanded field line topology to provide the best data-

theory comparison. Let us examine which provides the best fit to the data.

4.2. Numerical Experiment Results

[34] The code was run for six cases: nominal field line profile with each of the three atmosphere choices and the other three field line profiles with the solar minimum atmosphere. A primary photoelectron spectrum was calculated taking into account the local solar zenith angle and attenuation of the photon flux through the slant path column above each point. Secondary electrons due to impact ionization (an energy loss term in the calculation) are also included as a source of electrons in the simulation. Each calculation was run until a steady state solution was achieved. All results shown below are from the altitude grid cell closest to 400 km along the southern leg of the field line (comparable to the location 1 data presented in Figures 3, 4a, 4b, and 5a).

[35] Figure 9 shows differential number fluxes for the three atmospheric density profile choices. Figure 9 (left) shows the unfiltered results, that is, the actual model calculations shown to the resolution of the numerical grid. As in Figure 4a, Figure 9a shows the pitch angle-averaged fluxes, while Figures 9b–9d show the energy pitch angle spectrograms. The two horizontal white dashed lines on each of the spectrogram plots denote the source cone pitch angle for each ionospheric foot point (assumed to be at 200 km). The source cone sizes are not identical because the field strength is larger along the northern leg than along the southern leg. Figure 9 (right) shows the filtered results, that is, the model calculations after undergoing pitch angle and energy averaging over the measurement resolution of MGS. The results are blurred compared with the unfiltered results, but the right plots of Figure 9 are directly comparable to the data plots in Figures 4a and 4b.

[36] There are significant differences among the three model results presented in Figure 9. The solar minimum atmospheric profile (Figures 9b and 9f) offers enough scattering targets to fill in the trapped zone in the 10 eV energy bin. With increasing energy the scattering efficiency for collisions decreases, and the trapped zone is more depleted at each higher-energy step. At 500 eV the electrons are just a few degrees of pitch angle into the trapped zone. The below solar minimum atmosphere (Figures 9c and 9g) does not offer enough scattering targets along the field line, and therefore the trapped zone is vastly underfilled compared to the observations. At 10 eV the fluxes drop by 4 orders of magnitude between the source cone and the middle of the trapped zone. At 500 eV the fluxes plummet immediately beyond the edge of the largest source cone. For the solar maximum atmosphere (Figures 9d and 9h), there are so many scattering targets along the field line that the trapped zone is filled to isotropy up to 200 eV. Even at 500 eV, the fluxes drop by less than a factor of 2 across the trapped zone.

[37] Note that the absolute magnitude of the source cone fluxes at the high-energy end of the spectrum agree quite well with the observed values, while the magnitude of the modeled fluxes at the low-energy end are higher than observed. A main reason for the discrepancy is believed to be that the observed fluxes at low energies are lower limits
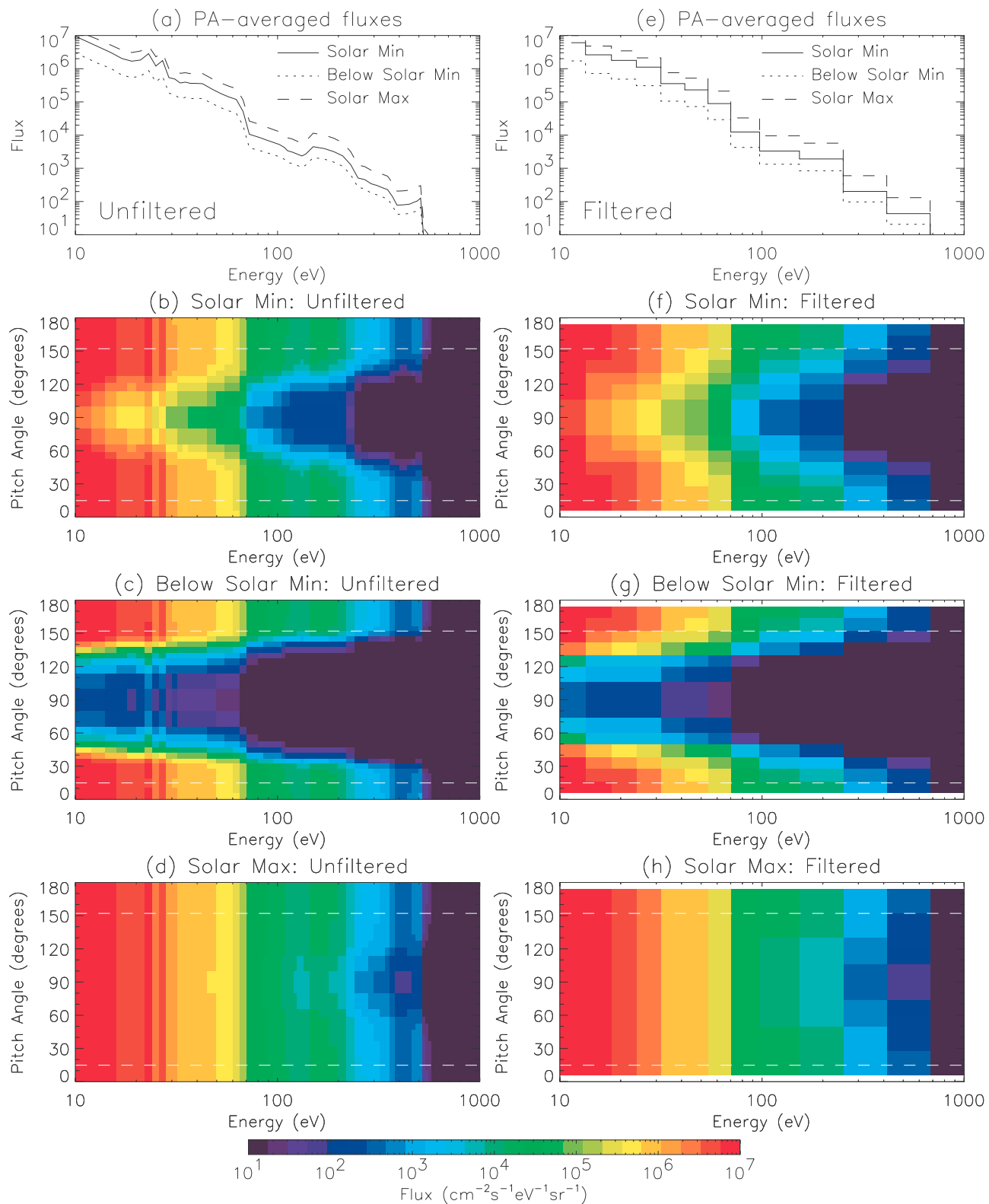
Figure 9.   Pitch angle-averaged energy spectra and energy pitch angle spectrograms for three simulation results with the nominal field line description and three different atmospheric density profiles. (left) "Unfiltered" results as produced from the model and (right) "filtered" results after averaging the model results into the MGS magnetometer/electron reflectometer pitch angle and energy bins are shown. These results are comparable to time 1 in Figures 2−5 (southern leg of the southern loop).

to the real values because of the gyrotropy selection criterion (discussed in section 2). It could also be due to differences between the solar photon flux used in the simulation compared to the real solar photon flux at Mars on the selected day.

[38] The solar minimum atmosphere provides the closest match of the three to the data in the low-energy ($E < 100$ eV) range, but the solar maximum atmosphere provides the closest match to the data in the high-energy range. The below solar minimum case is out of contention as a possible match for the data. The disparity of the comparisons for low and high energies is a puzzle. Given that the collisional processes included in the simulations (elastic and inelastic scattering/loss with the atmospheric neutrals and Coulomb scattering/loss with the already thermalized ions and electrons) all have decreasing efficiency at higher energies, it is expected that the high-energy electrons would show a larger depletion in the trapped zone than the low-energy electrons. The observations, however, show the reverse case. The most probable explanation is that the solar minimum atmosphere is the correct choice and there are other scattering processes preferentially acting on the high-energy electrons. The most likely candidate for the additional energy-dependent scattering process is wave-particle interactions between the electrons and whistler mode plasma waves. Under the proper conditions, whistler mode waves have been shown to be effective at scattering electrons in the hundreds of eV energy range while not affecting the lower-energy particles [e.g., *Liemohn et al.*, 1997b]. Whistler waves have been observed upstream of the bow shock of Mars [*Brain et al.*, 2002].

[39] Another possibility for the scattering process is violation of the first adiabatic invariant as the electrons pass through the high-altitude portion of the field line [e.g., *Speiser*, 1965; *Sergeev and Malkov*, 1988; *Anderson et al.*, 1997]. Such nonadiabatic scattering occurs because of a loss of magnetization, and strong pitch angle scattering occurs when the gyroradius (r_g) is greater than the radius of curvature (R_C) of the field line. This scattering has been identified as a cause of isotropic precipitation from the Earth's magnetotail [e.g., *Sergeev et al.*, 1993; *Delcourt et al.*, 1996] and in Jupiter's magnetodisc [e.g., *Birmingham*, 1984]. For the three field line configurations shown in Figure 8, the minimum R_C is 38 km for the nominal line, 49 km for the compressed line, and 35 km for the inflated line. For the B field strengths at the minimum R_C locations a 100 eV electron has r_g of 1.3, 0.84, and 1.7 km for the nominal, compressed, and inflated lines, respectively. The ratio of r_g/R_{Cmin} for 100 eV electrons is therefore 0.02 to 0.05. According to *Anderson et al.* [1997] such values result in $\Delta M/M$ of 10^{-5} to 10^{-4}, where M is the first adiabatic invariant $M = mv_\perp^2/2B$. Thus, at the very most, a 100 eV electron at small pitch angles (so that $\sin \alpha \approx \alpha$) would have a 1% change in its pitch angle as it passes through the region of minimum curvature. Because the particles originate in the source cone and are only making a single pass along the field line, it is unlikely that this process is responsible for filling the trapped zone at high energies. However, the calculation above is only a cursory evaluation, and a true test of this mechanism would require inclusion of an appropriate pitch angle diffusion coefficient in the model.

[40] Figure 10 shows the results for the remaining three simulation cases. The format is identical to that of Figure 9. The constant B field results (Figures 10b and 10f) are nearly isotropic at all energies. Such a result is expected, as there is no pitch angle focusing along the field line. Note that the two source cone edges are coincident at 90° pitch angle. There is some pitch angle variation in the results. There are two main reasons for the variation: (1) The primary photoelectron sources in the two ionospheric foot points have slightly different intensities, and (2) the electrons with pitch angles closer to 90° move slower along the field line and thus undergo more collisions (energy loss) than those that are more field-aligned (pitch angles closer to 0° or 180°). The inflated line results (Figures 10c and 10g) are quite similar to the results for the nominal field line configuration (Figures 9b and 9f). A close comparison of the two sets of plots reveals that the inflated line simulation has a slightly less depleted trapped zone than the nominal case. The extra filling is because the flight path is longer and the effective "optical depth" of scattering targets is larger for the inflated field line configuration. The compressed field line results (Figures 10d and 10h) are also quite similar to the nominal case. Close inspection reveals almost no difference in the results at all energies. The similarity is because the optical depth through the upper atmosphere is nearly identical for the compressed and nominal field line simulations.

[41] One thing that is clear from Figure 10 is that a constant magnetic field strength along the field line does not yield results that match the observations. It is difficult to say, however, which of the three magnetic field topologies best represent the real field line on the selected day. Therefore it is useful to introduce a new type of data product: the ratio of the highest flux value (across all pitch angles) at a given energy to the lowest flux value at that energy. The ratio can be calculated for all energies and for the observed data as well as the numerical results.

[42] Figure 11 shows maximum-to-minimum flux ratios for the location 1 data and five of the simulation results. The below solar minimum curve is well beyond the top of the scale shown in Figure 11, even at 10 eV. It is seen that the inflated line configuration provides the best fit to the observed flux ratios below 30 eV, where the bulk of the photoelectrons are located. Deviation of the inflated line simulation ratio from the observed ratio begins at energies above 30 eV. The observed ratio remains between 2 and 4 regardless of energy. Comparing Figure 11 with Figure 5a, it is seen that the data-derived flux ratio at low energies is reflecting the ratio of the source cone flux level to the trapped zone flux level. At high energies the maximum and minimum values could be at any pitch angle. That is, the high-energy electrons are quasi-isotropic, with seemingly random variations across the pitch angle range. Therefore even though the "solar maximum" curve matches the data curve in the hundreds of eV range, the similarity is coincidental because the pitch angle distributions are actually quite different. Regardless, a maximum/minimum flux ratio of 2 to 4 for all energies is not expected from collisional processes alone, as seen from the simulation results. The breakpoint between the data curve and the expanded field line result curve contains information about the additional scattering process (for instance, the plasma wave intensity
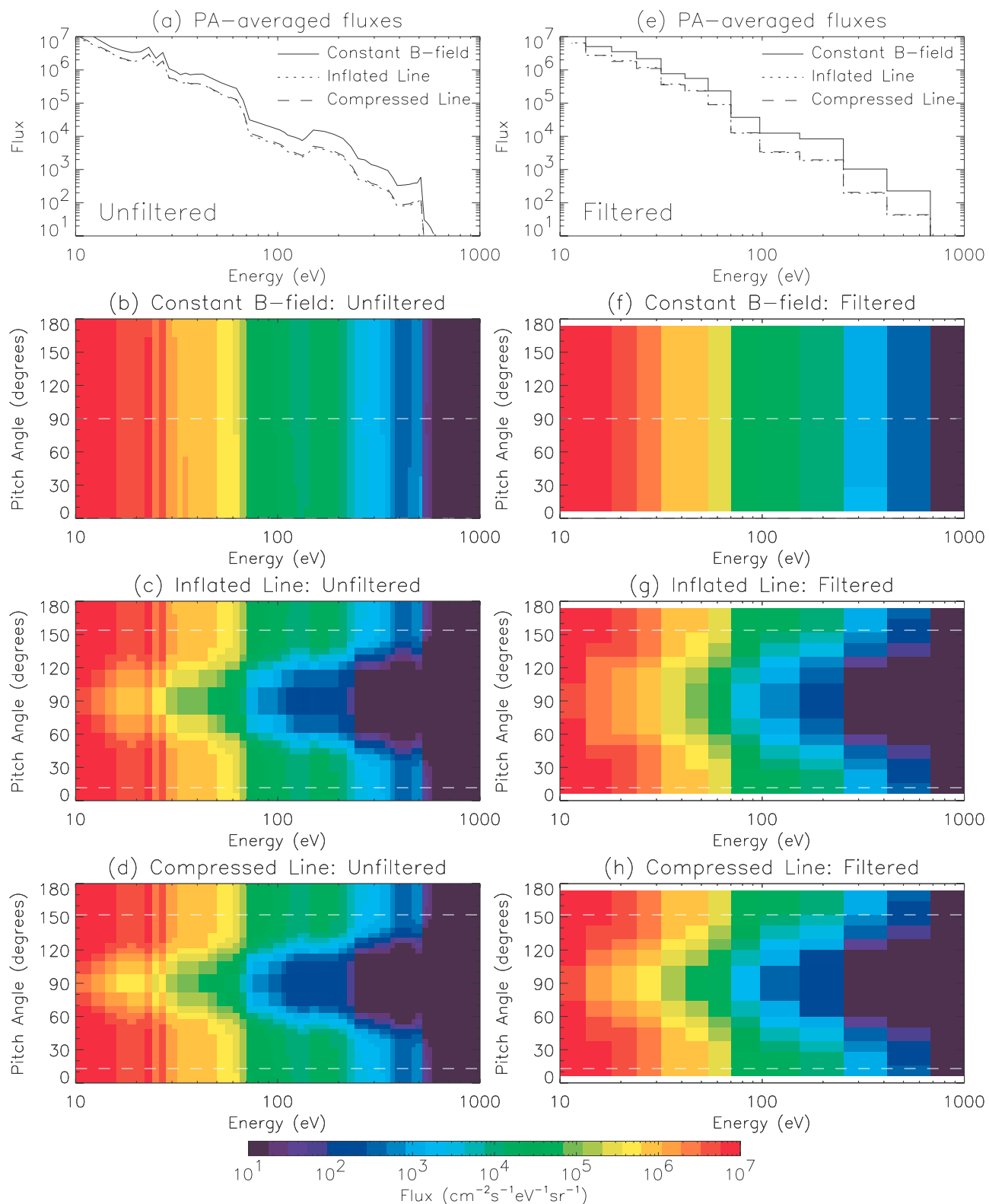
Figure 10. Like Figure 9 except for three simulation results with the nominal (solar minimum) atmosphere and three different magnetic field descriptions.
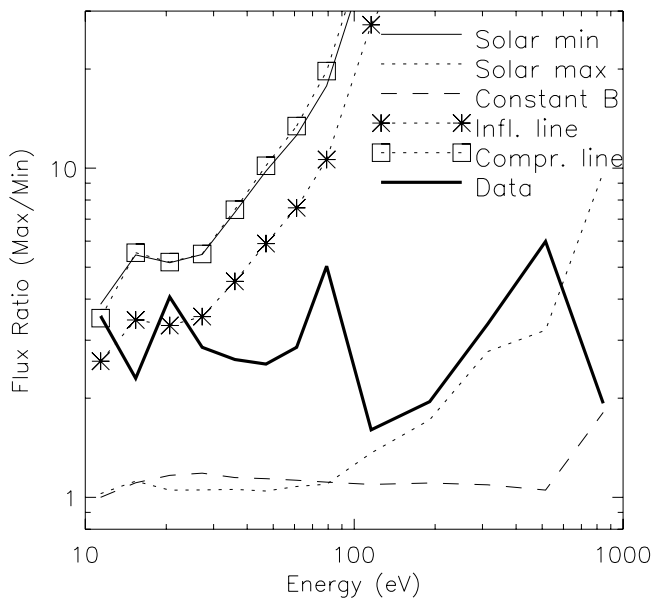
Figure 11. Ratios of the maximum to the minimum flux value from the pitch angle distribution for each energy bin from all of the simulation results and the observations (bold solid line). Note that the simulation results are from the filtered versions for direct comparison with the data. The below solar minimum atmosphere case is not shown because it is several orders of magnitude above the top of the scale.

versus frequency and the average wave normal angle), but a detailed investigation of the extra process is beyond the scope of this initial study.

5. Conclusion

[43] It has been shown that the electron velocity distributions in the crustal field regions above Mars contain many interesting features, including pitch angle anisotropies. Such features provide information about the magnetic field topology and the thermospheric/ionospheric density structure. In order to numerically examine the observed distributions a time-dependent, multistream electron transport model was employed. This model allows for the variation of the magnetic field strength along the field line, taking into account the pitch angle focusing and broadening resulting from the B field changes. Several simulations were conducted to investigate the anisotropy of one of the measured distributions, and it was determined that the best fit to the data was for an inflated model field line and solar minimum atmospheric/ionospheric density values. A proxy for the solar wind dynamic pressure indicates that the pressure for the chosen orbit was unusually low. Thus expansion of the field line is highly likely, and the result seems reasonable.

[44] It should be noted that there is a uniqueness issue with the data-theory comparison. That is, examination of Figure 11 reveals that an atmospheric density profile somewhere between aphelion solar minimum and perihelion solar maximum conditions would yield a flux ratio similar to the observed values in the low-energy range. While such a result is possible to obtain, it is believed that the solar

wind pressure proxy provides stronger evidence that the field line was inflated rather than the atmosphere being denser above 400 km.

[45] There is also the issue of the discrepancy in the observed and modeled flux ratios at high energies. The observed distributions are not consistent with purely collisional processes, which will scatter the low-energy electrons more than the high-energy ones. It is thought that an extra scattering process is preferentially isotropizing the electrons at high energies, and a good candidate exists in resonant interactions with plasma waves. Other possibilities exist, however, and a thorough test of these mechanisms should be conducted.

[46] Another finding is that the simulation results with a constant magnetic field strength along the model field line yield an unrealistic electron distribution. Such a result is expected because the field strength varies dramatically over the length of the field line. However, the standard approach to electron transport modeling at Mars up until now has been to use a two-stream code, which reduces the pitch angle distribution down to two bins. The study presented here indicates that such an approach is inadequate for the crustal field lines at Mars.

References

Acuña, M. H., et al., Mars Observer magnetic fields investigation, *J. Geophys. Res.*, *97*, 7799, 1992.

Acuña, M. H., et al., Magnetic field and plasma observations at Mars: Initial results of the Mars Global Surveyor Mission, *Science*, *279*, 1676, 1998.

Acuña, M. H., et al., Global distribution of crustal magnetization discovered by the Mars Global Surveyor MAG/ER experiment, *Science*, *284*, 790, 1999.

Acuña, M. H., et al., Magnetic field of Mars: Summary of results from the aerobraking and mapping orbits, *J. Geophys. Res.*, *106*, 23,403, 2001.

Anderson, B. J., R. B. Decker, N. P. Paschalidas, and T. Sarris, Onset of nonadiabatic particle motion in the near-Earth magnetotail, *J. Geophys. Res.*, *102*, 17,553, 1997.

Arkani-Hamed, J., A 50-degree spherical harmonic model of the magnetic field of Mars, *J. Geophys. Res.*, *106*, 23,197, 2001.

Arkani-Hamed, J., An improved 50-degree spherical harmonic model of the magnetic field of Mars derived from both high-latitude and low-latitude data, *J. Geophys. Res.*, *107*(E10), 5083, doi:10.1029/2001JE001835, 2002.

Birmingham, T. J., Pitch angle diffusion in the Jovian magnetodisc, *J. Geophys. Res.*, *89*, 2699, 1984.

Bougher, S. W., R. E. Dickinson, R. G. Roble, and E. C. Ridley, Mars thermospheric general circulation model: Calculations for the arrival of Phobos at Mars, *Geophys. Res. Lett.*, *15*, 1511, 1988.

Bougher, S. W., D. M. Hunten, and R. G. Roble, CO_2 cooling in terrestrial planet atmospheres, *J. Geophys. Res.*, *99*, 14,609, 1994.

Bougher, S. W., S. Engel, D. P. Hinson, and J. M. Forbes, Mars Global Surveyor Radio Science electron density profiles: Neutral atmosphere implications, *Geophys. Res. Lett.*, *28*, 3091, 2001.

Brain, D. A., F. Bagenal, M. H. Acuña, J. E. P. Connerney, D. H. Crider, C. Mazelle, D. L. Mitchell, and N. F. Ness, Observations of low-frequency electromagnetic plasma waves upstream from the Martian bow shock, *J. Geophys. Res.*, *107*(A6), 1076, doi:10.1029/2000JA000416, 2002.

Cain, J. C., B. B. Ferguson, and D. Mozzoni, An $n = 90$ internal potential function of the Martian crustal magnetic field, *J. Geophys. Res.*, *108*(E2), 5008, doi:10.1029/2000JE001487, 2003.

Chen, R. H., T. E. Cravens, and A. F. Nagy, The Martian ionosphere in light of the Viking observations, *J. Geophys. Res.*, *83*, 3871, 1978.

Connerney, J. E. P., M. H. Acuña, P. J. Wasilewski, N. F. Ness, H. Reme, C. Mazelle, D. Vignes, R. P. Lin, D. L. Mitchell, and P. A. Cloutier, Magnetic lineations in the ancient crust of Mars, *Science*, *284*, 794, 1999.

Connerney, J. E. P., M. H. Acuña, P. J. Wasilewski, G. Kleteschka, N. F. Ness, H. Reme, R. P. Lin, and D. L. Mitchell, The global magnetic field

of Mars and implications for crustal evolution, *Geophys. Res. Lett.*, *28*, 4015, 2001.

Crider, D., et al., Evidence of electron impact ionization in the magnetic pileup boundary of Mars, *Geophys. Res. Lett.*, *27*, 45, 2000.

Crider, D. H., et al., Observations of the latitude dependence of the location of the Martian magnetic pileup boundary, *Geophys. Res. Lett.*, *29*(8), 1170, doi:10.1029/2001GL0138604, 2002.

Delcourt, D. C., J.-A. Sauvaud, R. F. Martin Jr., and T. E. Moore, On the nonadiabatic precipitation of ions from the near-Earth plasma sheet, *J. Geophys. Res.*, *101*, 17,409, 1996.

Fox, J. L., Cross sections and reaction rates of relevance to aeronomy, *U. S. Natl. Rep. Int. Union Geod. Geophys. 1987–1990, Rev. Geophys.*, *29*, 1110, 1991.

Fox, J. L., and A. Dalgarno, Electron energy deposition in carbon dioxide, *Planet. Space Sci.*, *27*, 491, 1979.

Fox, J. L., P. Zhou, and S. W. Bougher, The Martian thermosphere/ionosphere at high and low solar activities, *Adv. Space Res.*, *17*(11), 203, 1996.

Gan, L., T. E. Cravens, and M. Horanyi, Electrons in the ionopause boundary layer of Venus, *J. Geophys. Res.*, *95*, 19,023, 1990.

Hinteregger, H. E., K. Fukui, and B. R. Gilson, Observational, reference and model data on solar EUV, from measurements on AE-E, *Geophys. Res. Lett.*, *8*, 1147, 1981.

Khazanov, G. V., and M. W. Liemohn, Non-steady-state ionosphere-plasmasphere coupling of superthermal electrons, *J. Geophys. Res.*, *100*, 9669, 1995.

Khazanov, G. V., M. A. Koen, Y. V. Konikov, and I. M. Sidorov, Simulation of ionosphere-plasmasphere coupling taking into account ion inertia and temperature anisotropy, *Planet. Space Sci.*, *32*, 585, 1984.

Khazanov, G. V., M. W. Liemohn, T. I. Gombosi, and A. F. Nagy, Non-steady-state transport of superthermal electrons in the plasmasphere, *Geophys. Res. Lett.*, *20*, 2821, 1993.

Liemohn, M. W., G. V. Khazanov, T. E. Moore, and S. M. Guiter, Self-consistent superthermal electron effects on plasmaspheric refilling, *J. Geophys. Res.*, *102*, 7523, 1997a.

Liemohn, M. W., G. V. Khazanov, and J. U. Kozyra, Guided plasmaspheric hiss interactions with superthermal electrons: 1. Resonance curves and timescales, *J. Geophys. Res.*, *102*, 11,619, 1997b.

Lin, R. P., D. L. Mitchell, D. W. Curtis, K. A. Anderson, C. W. Carlson, J. McFadden, M. H. Acuña, L. L. Hood, and A. Binder, Lunar surface magnetic fields and their interaction with the solar wind: Results from Lunar Prospector, *Science*, *281*, 1480, 1998.

Link, R., Energetic electrons in the ionosphere and exosphere of Mars, *Eos Trans. AGU*, *80*(46), Fall Meet. Suppl., F874, 1999.

Luhmann, J. G., and L. H. Brace, Near-Mars space, *Rev. Geophys.*, *29*, 121, 1991.

Ma, Y., A. F. Nagy, K. C. Hansen, D. L. DeZeeuw, and T. I. Gombosi, Three-dimensional multispecies MHD studies of the solar wind interaction with Mars in the presence of crustal fields, *J. Geophys. Res.*, *107*(A10), 1282, doi:10.1029/2002JA009293, 2002.

Mantas, G. P., and W. B. Hanson, Photoelectron fluxes in the Martian ionosphere, *J. Geophys. Res.*, *84*, 369, 1979.

Mitchell, D. L., et al., Oxygen Auger electrons observed in Mars' ionosphere, *Geophys. Res. Lett.*, *27*, 1871, 2000a.

Mitchell, D. L., R. P. Lin, H. Rème, P. A. Cloutier, J. E. P. Connerney, M. H. Acuña, and N. F. Ness, The shape of Mars' ionosphere and its response to solar activity and crustal magnetic fields: Observations by the MGS electron reflectometer, *Eos Trans. AGU*, *81*(48), Fall Meet. Suppl., Abstract P61A-05, 2000b.

Mitchell, D. L., et al., Probing Mars' crustal magnetic field and ionosphere with the MGS electron reflectometer, *J. Geophys. Res.*, *106*, 23,419, 2001.

Nagy, A. F., and P. M. Banks, Photoelectron fluxes in the ionosphere, *J. Geophys. Res.*, *75*, 6260, 1970.

Ness, N. F., M. H. Acuña, J. E. P. Connerney, A. J. Kliore, T. K. Breus, A. M. Krymskii, P. Cloutier, and S. J. Bauer, Effects of magnetic anomalies discovered at Mars on the structure of the Martian ionosphere and solar wind interaction as follows from radio occultation experiments, *J. Geophys. Res.*, *105*, 15,991, 2000.

Purucker, M., D. Ravat, H. Frey, C. Voorhies, T. Sabaka, and M. Acuña, An altitude-normalized magnetic map of Mars and its interpretation, *Geophys. Res. Lett.*, *27*, 2449, 2000.

Rohrbaugh, R. P., J. S. Nisbet, E. Bleuler, and J. R. Herman, The effect of energetically produced O_2^+ on the ion temperatures of the Martian thermosphere, *J. Geophys. Res.*, *84*, 3327, 1979.

Sergeev, V. A., and M. V. Malkov, Diagnostics of the magnetic configuration of the plasma layer from measurements of energetic electrons above the ionosphere, *Geomagn. Aeron.*, *28*, 549, 1988.

Sergeev, V. A., M. Malkov, and K. Mursula, Testing the isotropic boundary algorithm method to evaluate the magnetic field configuration in the tail, *J. Geophys. Res.*, *98*, 7609, 1993.

Seth, S. P., S. A. Haider, and K. I. Oyama, Photoelectron flux and nightglow emissions of 5577 and 6300 Å due to solar wind electron precipitation in Martian atmosphere, *J. Geophys. Res.*, *107*(A10), 1324, doi:10.1029/2001JA000261, 2002.

Solomon, S. C., S. M. Bailey, and T. N. Woods, Effect of solar soft X-rays on the lower ionosphere, *Geophys. Res. Lett.*, *28*, 2149, 2001.

Speiser, T. Q., Particle trajectories in model current sheets: 1. Analytical solutions, *J. Geophys. Res.*, *70*, 4219, 1965.

Sung, K., and J. L. Fox, Electron impact cross sections for use in modeling the ionospheres/thermospheres of the Earth and planets, *Eos Trans. AGU*, *81*(48), Fall Meet. Suppl., Abstract SA52A-11, 2000.

Szego, K., Possible effects of the Martian crustal magnetization on its magnetosphere, *Geophys. Res. Lett.*, *27*, 1343, 2000.

Vennerstrom, S., N. Olsen, M. Purucker, M. H. Acuña, and J. C. Cain, The magnetic field in the pile-up region at Mars, and its variation with the solar wind, *Geophys. Res. Lett.*, *30*(7), 1369, doi:10.1029/2003GL016883, 2003.

————————————

J. L. Fox, Department of Physics, Wright State University, Dayton, OH 45435-0001, USA. (fox@platmo.phy.wright.edu)

M. W. Liemohn, Y. Ma, and A. F. Nagy, Space Physics Research Laboratory, University of Michigan, 2455 Hayward Street, Ann Arbor, MI 48109-2143, USA. (liemohn@umich.edu; yingjuan@umich.edu; anagy@umich.edu)

D. L. Mitchell, Space Sciences Laboratory, University of California, Berkeley, Laboratory Centennial at Grizzly Peak, Berkeley, CA 94720-7450, USA. (mitchell@ssl.berkeley.edu)

T. W. Reimer, Physics Department, Harvey Mudd College, Claremont, CA 91711, USA. (treimer@hmc.edu)